AIAA 96-2274
High Reynolds Number Analysis of an Axisymmetric Afterbody with Flow Separation

John R. Carlson
David E. Reubush
NASA Langley Research Center
Hampton, VA

19th AIAA Advanced Measurement and Ground Testing Technology Conference
June 17-20, 1996 / New Orleans, LA

HIGH REYNOLDS NUMBER ANALYSIS OF AN AXISYMMETRIC AFTERBODY WITH FLOW SEPARATION

John R. Carlson*
David E. Reubush**
NASA Langley Research Center
Hampton, VA 23681

ABSTRACT

The ability of a three-dimensional Navier-Stokes method, PAB3D, to predict nozzle afterbody flow at high Reynolds number was assessed. Predicted surface pressure coefficient distributions and integrated afterbody drag are compared with experimental data obtained from the NASA-Langley 0.3 m Transonic Cryogenic Tunnel. Predicted afterbody surface pressures matched experimental data fairly closely. The change in the pressure coefficient distribution with Reynolds number was slightly over-predicted. Integrated afterbody drag was typically high compared to the experimental data. The change in afterbody pressure drag with Reynolds number was fairly small. The predicted point of flow separation on the nozzle was slightly downstream of that observed from oil-flow data at low Reynolds numbers and had a very slight Reynolds number dependence, moving slightly further downstream as Reynolds number increased.

INTRODUCTION

Potential differences between the data obtained through typically low Reynolds number scale model wind-tunnel testing and that of full scale has historically been a concern and the present advanced subsonic and high-speed research programs have renewed this attention. In particular, concern about potential Reynolds number effects on drag has been focused in the area of propulsion-airframe integration (PAI) testing, where high afterbody slopes and long boundary-layer runs result in large viscous effects on the nozzle boattail. Additionally, extensive use of computational fluid dynamics (CFD), from incompressible panel methods through advanced Navier-Stokes methods, for preliminary design studies in these same transport programs, with no direct evidence of their ability to predict correctly the effects due to Reynolds number, have resulted in similar concerns.

Previous to the development of cryogenic test techniques for achieving high Reynolds numbers in wind tunnel test facilities little fundamental research data had been available for the evaluation of any CFD methods for their ability to predict Reynolds number effects in PAI. However, a number of years ago, during the developmental phase of cryogenic testing techniques at the NASA Langley Research Center; two sets of simple axisymmetric nacelle models were built and tested in what was then known as the 1/3 m Pilot Transonic Cryogenic Tunnel (now the 0.3 m Transonic Cryogenic Tunnel); thereby obtaining some of the first test data for a number of nozzle-boattail configurations over a wide Reynolds number range, refs. 1-4. The 8 inch long (forebody) geometry of most of these models was, by design, a scaled down version of a 48 inch long model that had been tested in the Langley 16-Foot Transonic Tunnel, thus providing additional comparisons of quality and repeatability of wind tunnel data between facilities, ref. 1.

The multiblock three-dimensional Navier-Stokes method PAB3D, refs. 5, 6, and 7, was used for all the calculations and utilized the algebraic Reynolds stress model of Shih, Zhu, and Lumley for turbulence simulation, refs. 8 and 9. Grid sensitivity was evaluated for afterbody pressure coefficients and integrated pressure drag using the performance package, ref. 10. Afterbody pressure coefficients and drag were compared with experimental data.

NOMENCLATURE

A_{max}	maximum body cross-sectional area, 0.78540 in^2
C_D	pressure drag coefficient, $F/q_\infty A_{max}$
C_p	pressure coefficient, $(p - p_\infty)/q_\infty$
d_m	body maximum diameter, 1.0 in.
L	length of body from nose to nozzle connect station, 8 or 16 in.
l	length of nozzle, in.
M_∞	free-stream Mach number
p	static pressure
p_∞	free-stream static pressure
q_∞	free-stream dynamic pressure

*Senior Scientist, Component Integration Branch, Aerodynamics Division. Senior Member AIAA.
**Acting Deputy Director, Hypersonic Vehicles Office. Associate Fellow AIAA.

N_{Re}	Reynolds number based on body length
u_∞	free-stream velocity
u	axial velocity
x	axial distance
y	lateral distance from model centerline
z	vertical or radial distance from model centerline
α	flow angle-of-attack, degrees
ϕ	angular location of pressure orifices, degrees

Subscripts

β	nozzle boattail component contribution
CL	centerline
exp	experiment
t	total conditions

DISCUSSION

Experimental Model and Data

The model used for this study was one of six models that were built for the original Reynolds number study, refs.1 and 2. Four models with differing boattail geometry with a length of 8 inches from the nose to the start of the boattail (characteristic length) and two models with a length of 16 inches were constructed. The boattail geometries had circular arc (2), circular arc-conic, or contoured cross-sections. This investigation utilized the circular arc with a length-to-maximum-diameter ratio (fineness ratio – l/d_m) of 0.8 boattail. Figure 1 is a photograph of the model mounted in the pilot tunnel. The nose of the model was a 28° cone, 1.7956 inches long fairing to the cylindrical body via a 1.3615 inch radius circular arc centered 2.125 inches downstream of the model leading edge and 0.8615 inches below the model centerline. The circular arc fairing is tangent at its endpoints to the conical nose (1.7956 inches from the nose) and cylindrical body (2.125 inches from the nose). The model was sting mounted with the diameter of the sting being equal to the model base diameter. The length of the constant diameter portion of the sting (6.70 inches measured from the nozzle connect station) was such that, based on the work of Cahn, ref. 11, there should be no effect of the sting flare downstream of the nozzle trailing edge on the boattail pressure distributions. The following is a tabulation of the non-dimensional orifice locations.

x/d_m for L/Dm = 8 at		
$\phi = 0°$	$\phi = 120°$	$\phi = 240°$
-0.2771	-0.2761	-0.2850
-0.0256	-0.0731	-0.0700
0.0770	0.0256	0.0345
0.1765	0.1287	0.1270
0.2750	0.2257	0.2260
0.3679	0.3240	0.3279
0.4675	0.4180	0.4200
0.5749	0.5166	0.5220
0.6698	0.6165	0.6376
0.7746	0.7280	0.7400
x/d_m for L/Dm = 16 at		
-0.4491	-0.4660	-0.4561
-0.1637	-0.2201	-0.1552
-0.0600	-0.1281	-0.0590
0.0337	-0.0260	0.0390
0.1268	0.0744	0.1342
0.2279	0.1729	0.2713
0.3210	0.2696	0.3718
0.4199	0.3679	0.4680
0.5231	0.4640	0.5749
0.6279	0.6758	0.7304

The models were constructed of cast aluminum with stainless-steel pressure tubes cast as an integral part of the model. The models were instrumented with 30 pressure orifices in three rows of 10 orifices each. The 1 inch diameter of the model physically precluded the placement of all 30 orifices along the same row. The tunnel has an octagonal test section with slots at the corners of the octagon and is essentially a scale model of the Langley 16-Foot Transonic Tunnel test section, ref. 12. The test medium for the cryogenic tunnel was nitrogen.

The total temperature and pressure of the pilot tunnel could be independently controlled. The experiment was conducted over a range of temperatures from approximately 117 K to 308 K and pressures from 1 to 5 times the standard atmospheric level. Any number of free stream total temperatures or pressures can result in identical settings of Reynolds number. From experiments conducted at several conditions which resulted in the same Reynolds number surface pressure coefficients and nozzle boattail drag were shown to be

similar regardless of the temperature/pressure combinations that created equivalent Reynolds numbers, ref. 4. Though data were obtained over the range of Mach number from 0.6 to 0.9, only the M = 0.6 data are compared with the CFD of this paper. The following is a table of conditions for experimental data obtained at M = 0.6 for the $L/d_m = 8$ model. One atmosphere is defined as 0.101325 MPa.

T_t, K	p_t, atm	$N_{Re} \times 10^{-6}$
117	5.00	43
117	4.00	34
117	3.00	26
117	2.50	21.5
117	2.00	17
117	1.50	13
117	1.30	11.5
308	5.00	11.5
308	3.80	8.5
308	3.14	7.0
308	2.50	5.5
308	1.25	3.0

Computational Procedure

Governing Equations. The code used was the general 3-D Navier-Stokes method PAB3D-Version 13G. This code has several computational schemes and different turbulence models that can be utilized, as described in more detail in references 6 and 8. The governing equations are the Reynolds-averaged simplified Navier-Stokes equations (RANS) obtained by neglecting all streamwise derivatives of the viscous terms. The resulting equations are written in generalized coordinates and conservation form. The implementation of the full three dimensional viscous stresses are reduced to thin-layer viscous assumptions, although full Navier-Stokes simulation is an option. The diffusion terms are centrally differenced and the inviscid flux terms are upwind differenced. Two finite volume flux-splitting schemes are used to construct the convective flux terms. The Roe upwind scheme with third order accuracy is used in evaluating the explicit part of the governing equations and the van Leer scheme is used to construct the implicit operator.

The user will typically utilize the Roe scheme procedure to sweep streamwise through the computational domain and the van Leer scheme for the solution of the cross-plane (i.e., i = constant) of a three dimensional problem. A single-cell wide, two-dimensional mesh defined with the i direction of the grid oriented in the conventional streamwise direction will typically converge slower using the Roe relaxation solution scheme compared to solving the equivalent problem with the van Leer scheme. Therefore the i and j directions of the 2-D mesh are swapped allowing the entire flowfield to be solved implicitly with each iteration. The explicit sweep is not used since only one cell exists in the i direction. The implicit scheme has the potential of a much higher rate of convergence and can provide a solution using less computational time.

Several near-wall models and compressibility corrections are available to be used with several formulations of linear two-equation k-ε turbulence model, (e.g. Standard, Jones & Launder, Yang & Shih). The k-ε turbulence model equations are uncoupled from the RANS equations and can be solved with a different time step than that of the principle flow solution. Version 13G of the PAB3D code used in this study has options for several algebraic Reynolds stress (ASM) turbulence simulations. The standard model coefficients of the k-ε equations were used as the basis for all the linear and non-linear turbulent simulations, ref. 13. Additionally, it is known that the eddy viscosity models produce inaccurate normal Reynolds stresses. Flat plate flow, as well as other more complex aerodynamic flows, are anisotropic. Successful implementation of the algebraic Reynolds stress models required the solution methodology for turbulent production term of the underlying linear turbulence calculations to be modified. Turbulence production depends on high order derivatives of the turbulent Reynolds stresses. Proper representation of the stresses should be provided by face centered values, rather than the cell centered values. Previous attempts to implement non-linear turbulence models in the context of a cell centered eddy viscosity model worked only for 2-D problems and was unable to resolve 3-D flows. The two non-linear turbulence models used in this paper are the theories by Shih, Zhu & Lumley, ref. 9, and by Gatski & Speziale, ref. 14. All flow solutions were developed with PAB3D-V13G using the standard formulation of linear k-ε as the basis for the algebraic Reynolds stress calculation. The damping function of Launder & Sharma, ref. 15, was used to control the near-wall behavior of k and ε was set to $2\upsilon((\partial\sqrt{k})/\partial n)^2$ at solid surfaces. Turbulent flow solutions using either the ASM or two-equation linear k-ε model requires 23 words per grid point. The code speed was 43 micro-seconds per grid point (Cray 2 time) solving ASM turbulent flow simulations.

The conservative patch interface package of Pao & Abdol-Hamid, ref. 7, enables the code to properly transmit information between mis-matched block interfaces. Integer-

to-one interfaces are considered a subset of the arbitrary block interface and do not need to be specified as such to the patching code. The patching program writes a connectivity database as a preprocessor prior to execution of the flow solver. Each entry to the patch database contains cell face areas and indices relating that cell with all other cells that will share momentum flux information. The database information is automatically re-allocated internal to the code during mesh sequencing. As a result, each block can be sequenced at different levels and the correct interface information is maintained at the cell level. However, it is important to note that features in the flow developed on one side of an interface should not be obliterated on the other side due to too severe a grid density mis-match.

Third-order continuity in transmitting the fluxes across block boundaries is maintained by the code; lower order continuity may be specified by the user if required. Equal cell size spacing on either side of an interface in directions normal to the interface must still be maintained regardless of the mesh sequencing level of the block.

Boundary Conditions. For this study, solid walls were treated as no-slip adiabatic surfaces. The solid wall boundary condition was satisfied by setting the momentum flux of the solid wall cell face to zero. The boundary conditions used for the internal nozzle flow path were fixed total pressure, total temperature and flow angle at the plenum block inflow face. A boundary condition for the Riemann invariants along the characteristics was specified for the external freestream inflow face and the lateral freestream outer boundary of the flow domain. An extrapolation boundary condition was applied on the downstream outflow face where both the free stream and the nozzle plume exit the computational domain. The axisymmetric flow assumption for the single-cell grids was implemented by placing flow symmetry conditions to the lateral side boundaries of the computational domain.

Solution Process. Total afterbody drag, nozzle pressure drag, and solution residual were used to determine the solution progress at the coarse (144), medium (122), and fine (111) grid levels of the axisymmetric afterbody. The 144 abbreviation means the number of i-cells, j-cells, and k-cells were, internal to the code, reduced by 1, 4, and 4 respectively to develop a coarse grid solution. Afterbody drag variance of less than 0.50 percent for several hundred iterations was achieved for all test cases.

Computational Grid Setup. The axisymmetric afterbody grid utilized H-O type mesh topology with all block dimensions that were sequencable by 4. The mesh was gridded with a single cell wide 5 degree wedge grid with the streamwise flow direction oriented along the j index to utilize the implicit flow solver in the code for faster solution convergence. Figures 2 through 4 are overall and detail views of the cell centered grid. The body was described using 100 cells extending from the leading edge of the nose to the nozzle connect station. There were 80 cells extending from the nozzle connect station to the nozzle boattail trailing edge.

The first cell height typically decreased with increasing Reynolds number of the freestream. The following schedule was used for the freestream conditions of M = 0.6 and T_t = 560° R and the model reference length of L/d_m = 8. These data are also plotted in figure 5 and are compared with a 1-D isentropic flat plate curve of the variation of the first cell height with Reynolds number for a flat plate (solid line) for a y^+ = 1.0. Therefore, the flow in the first cell center above the surface using a grid generated with guidance from flat plate theory would then be y^+ = 0.5.

$N_{Re} \times 10^{-6}$	p_{t0}, psi	h_1, in $\times 10^6$	y^+
11	73.	20	0.50
25.6	171.	8	0.27
43.1	287.	2	0.18
100.0	665.	2	0.39

The first physical cell height for the different Reynolds number grids for this model are indicated by the solid circles. The open circle symbols are the y^+ of the flow and show that the y^+ for converged solutions were generally between 0.5 and 0.18. The low Reynolds number grid calculation was done at y^+ = 0.5. The ASM turbulence simulations have better convergence trends when at least 2 cells are below y^+ = 1. Therefore, for the higher Reynolds number grids the first cell spacing was slightly below the flat plate predictions. The range of acceptability is generally between a y^+ of 0.2 and 0.5, hence the two higher Reynolds number grids actually had the same physical spacing but the y^+ was still inside the acceptable range.

Results

Figures 6 through 10 are the sensitivity of the CFD method to grid density with Reynolds number. Figure 11 is the change in predicted nozzle pressure coefficient distribution with Reynolds number. Figure 12 shows the experimen-

tal trend in nozzle pressure coefficients with Reynolds number. Figure 13 is a comparison of CFD with experimental data obtained in two different wind tunnels around the Reynolds number of 5 million. Figure 14 is a comparison of predicted and experimental nozzle pressure drag with Reynolds number and figure 15 is a comparison of two analytic techniques for predicting skin friction drag on the nozzle boattail with Reynolds number. Figure 16 is the predicted trend of the point flow separation on the nozzle with Reynolds number. Figure 17 is a photograph of an oil-flow at M = 0.85 and figure 18 is an analysis of integrated pressure drag error build-up between experimental data and CFD.

In figures 6 through 10 repeat experimental data points were plotted along with solutions at three grid levels (coarse (144), medium (122), and fine (111)) to evaluate the experimental data scatter and CFD grid sensitivity, respectively. The coarse grid computation was consistently low in the recovery pressure in the region of separated flow downstream of $x/d_m = 0.55$ for the complete Reynolds number range. Grid convergence was closely attained as the medium and fine grids were very similar, but not identical, at each of the Reynolds numbers. The level of flow expansion around the boattail shoulder was predicted. The pressure recovery was generally underpredicted at Reynolds numbers below 40 million, while the pressure level was generally matched above 40 million.

Figures 11 and 12 show the predicted change in nozzle surface pressure coefficients with Reynolds number computationally and experimentally, respectively. The experimental data curves are smoothed, averaged data over the three angular rows of orifices. In general, the CFD shows lower peak pressure coefficients at the flow expansion peak near $x/d_m = 0.15$ with increasing Reynolds number. Also higher recovery pressures in the region of separated flow downstream of approximately $x/d_m = 0.6$ are predicted with increasing Reynolds number. These trends were qualitatively the same with the experimental data, though the CFD overpredicted the change in recovery pressure in the separated flow region with Reynolds number.

A comparison of CFD (computed for the 5.7 million Reynolds number of the cryogenic tunnel data) with experimental data obtained from both the 16-foot Transonic Tunnel and the cryogenic Tunnel and two different wind tunnel models, ref. 16, is shown in figure 13. The differences in the flow due to the Reynolds number variation 3.6 million to 6.9 million should not effect the validity of the comparison. There are data for the 16 inch model from both tunnels, refs. 1 and 16, and data for the 8 inch model from just the 0.3 m tunnel, ref. 1. In general there does not appear to be a significant facility related difference in the pressure coefficient distributions. As mentioned in the previous section concerning grid sensitivity at the different Reynolds numbers, the CFD solution captures the flow expansion around the boattail shoulder fairly well, but slightly under-predicts the pressure recovery in the separated flow region downstream of $x/d_m = 0.5$ at this low a Reynolds number.

Figure 14 is a comparison of predicted nozzle boattail pressure drag coefficients with several experimental data sets. Like before, data from both the 0.3 m and 16-foot tunnels for several different models with the same nozzle boattail geometry are presented. Additionally, data from the 48 inch model with the same boattail geometry, ref. 17, is included. In general, the predicted pressure drag was higher than the data obtained from the 0.3 m facility, ref. 1. A better comparison is obtained with the 16-foot data which are the open triangle, diamond, (ref. 16) and x symbols, ref. 17, at 11 million Reynolds number and below. The open diamond in figure 14 is the integrated pressure drag obtained from the open circle symbols of figure 13. The open square around 6 million Reynolds number in figure 14 is the integrated pressure drag obtained from the solid circle symbols of figure 13, which appear fairly interspersed with the open circles. Reference 1 noted that very slight differences in pressure coefficient distributions appear to induce significant shifts in the level of pressure drag. The issue of assigning areas for the pressure-area integration process will be dealt with in a subsequent section. Also included in Figure 14 is a comparison of predicted nozzle boattail pressure drag for the 105 million Reynolds number test condition utilizing two alternative turbulence models, a linear model and that of Gatski and Speziale. There was not a significant difference in the drag coefficients predicted by the three methods.

A related issue when comparing CFD with experimental data is the assessment of skin friction drag. Typically the experiment assigns a wetted area to a portion of the model and, with the assumptions of constant Mach number and measured free-stream conditions, a flat-plate equivalent skin friction coefficient is calculated. The computational method has available considerably more information concerning the local flow on the model and could theoretically make an exact calculation of the skin friction forces. Three significant factors are accounted for in the computational method. First the stream wise variation in the local viscous stress at the wall can be calculated. Second, the effect of flow separation occurring on the latter 40 percent of the boattail can be bet-

ter accounted. Lastly, due to the curvature of the boattail, the component forces of the skin friction can be separately accounted. Despite these differences, the calculated skin-friction drag compared to the estimation from the wind tunnel investigation was roughly 5 boattail drag counts off at 5 million Reynolds number and 2 boattail drag counts off at 100 million Reynolds number, shown in figure 15.

Figure 16 is a comparison of predicted point of flow separation on the boattail compared to flow visualization data obtained in the 16-Foot tunnel. Flow visualization for this model were only available at approximately 12 million Reynolds number. The 8, 16, and 48 inch models were run computationally and are shown by the solid symbols. The point of flow separation experimentally was determined from picking points from photographs of oil-flow runs in the 16-Ft. tunnel. The point of flow separation computationally was the sign reversal of the local skin friction coefficient. Though no statement can be made concerning the experimental trend of the point of flow separation with Reynolds number for this model, computationally, a slight downstream shift in the separation point is observed with increasing Reynolds number. At 12 million Reynolds number, the CFD is slightly downstream of the experimentally estimated point. Figure 17 is a photograph of the oil flow over the solid plume model at M = 0.6. As can be observed by the mildly wandering dark line part way down the nozzle boattail, some three-dimensionality existed in this flow that was not in the computational solution. The dark line is assumed to be the flow separation point and the variation in location was estimated and is denoted by the vertical spread in open triangle symbols in figure 16.

As an attempt to clarify the difference between the integrated pressure drag on the boattail computationally compared with the experimental data when the pressure coefficient distributions appear fairly similar, several methods of integrating the computational data were investigated. The CFD drag numbers plotted in figure 14 were obtained by using the areas and pressures obtained directly from the computational grid. Due to the availability of the experimental areas used for the pressure integration, tabulated below, interpolated CFD pressure data were obtained at the exact experimental orifice locations and subsequently integrated using the experimental areas. The open circle symbols in figure 18 are the experimental data and the x symbols are the interpolated CFD solutions at the same physical locations. The filled diamonds are the difference between the CFD and experimental pressure coefficients multiplied by the axial area for that orifice location. Several locations have a large difference between the CFD and experiment but a very small projected area so the combination makes little difference in the error. The flow further downstream, between $x/d_m = 0.2$ to 0.5, experiences a rapid recompression trend that, though there is only a very slight downstream shift in the predicted recompression, created a consistently positive increment between the data and CFD. This difference multiplied by the increasing axial area contribution biased the predicted pressure drag. Overall, while there appeared to be a good comparison between the pressure coefficient data, the integrated drag numbers can be substantially different.

Areas for $L/D_m = 16$ at		
$\phi = 0°$	$\phi = 120°$	$\phi = 240°$
0.0	0.0	0.0
0.0	0.0	0.0
0.0	0.0	0.0
0.00051	0.00051	0.00051
0.0	0.00999	0.01366
0.02354	0.01858	0.01346
0.03332	0.01346	0.01880
0.04049	0.01880	0.02369
0.05384	0.02369	0.05487
0.05493	0.05705	0.10745

A comparison of the integrated drags obtained from experiment, CFD, and CFD using the experimental areas for four values of Reynolds number can be found in the following table. As can be seen, the CFD consistently predicted highter drag than the experiment, no matter which area assignment was used.

$N_{Re} \times 10^{-6}$	$C_{D_{exp}}$	$C_{D_{CFD}}$	$C_{D_{CFD}}$ exp area
25.6	0.0123	0.0214	0.0218
43.1	0.0100	0.0208	0.0274
67.0	0.0118	0.0184	0.0194
105.0	0.0102	0.0181	0.0189

However, it must be pointed out that these drag values are for an isolated nacelle and when applied to an actual aircraft the drag coefficients would be relatively lower. If the rule of thumb that when applied to a typical fighter the drag from an isolated nacelle should be divided by 20 is used the

next table results. With one exception, the drag predicted by CFD is within 5 airplane drag counts of that from the experiment, reasonably good agreement.

$N_{Re} \times 10^{-6}$	$C_{D_{exp}}$	$C_{D_{CFD}}$	$C_{D_{CFD}}$ exp area
25.6	0.0006	0.0011	0.0011
43.1	0.0005	0.0010	0.0014
67.0	0.0006	0.0009	0.0010
105.0	0.0005	0.0009	0.0009

SUMMARY

The ability of a three-dimensional Navier-Stokes method, PAB3D, to predict nozzle afterbody flow at high Reynolds number was assessed. Predicted surface pressure coefficient distributions and integrated afterbody drag are compared with experimental data obtained primarily from the NASA-Langley 0.3 m Transonic Cryogenic Tunnel with some data from the Langley 16-Foot Transonic Tunnel. Predicted afterbody surface pressures matched experimental data fairly closely. The change in the pressure coefficient distribution with Reynolds number was slightly over-predicted. Integrated afterbody drag was typically high compared to the experimental data. The change in afterbody pressure drag with Reynolds number was fairly small. The predicted point of flow separation on the nozzle was slightly downstream of that observed from oil-flow data at low Reynolds numbers and had a very slight Reynolds number dependence, moving slightly further downstream as Reynolds number increased.

REFERENCES

1. Reubush, D. E. and Putnam, L. E. : An Experimental and Analytical Investigation of the Effect on Isolated Boattail Drag of Varying Reynolds Number up to 130×10^6. NASA TN D-8210, May 1976.

2. Reubush, D. E.: The Effect of Reynolds Number on Boattail Drag. AIAA-75-63, AIAA 13th Aerospace Sciences Meeting, January 20-22, 1975.

3. Reubush, D. E.: The Effect of Reynolds Number on Boattail Drag of Two Wing-Body Configurations. AIAA-75-1294, AIAA/SAE 11th Joint Propulsion Conference, September 29-October 1, 1975.

4. Reubush, David E.: Experimental Investigation to Validate Use of Cryogenic Temperatures to Achieve High Reynolds Numbers in Boattail Pressure Testing. NASA TM X-3396, August, 1976.

5. Abdol-Hamid, K. S.: A Multiblock/Multizone Code (PAB3D-v2) for the Three-Dimensional Navier-Stokes Equations: Preliminary Applications, NASA CR-182032, October 1990.

6. Abdol-Hamid, K. S.; Carlson, J. R.; and Lakshmanan, B.: Application of Navier-Stokes Code PAB3D to Attached and Separated Flows for Use With k-ε Turbulence Model, NASA TP-3480, 1994.

7. Abdol-Hamid, K. S.; Carlson, J. R.; and Pao, S. P.: Calculation of Turbulent Flows Using Mesh Sequencing and Conservative Patch Algorithm. AIAA 95-2336, 31st. Joint Propulsion Conference, July 1995.

8. Abdol-Hamid, K. S.: Implementation of Algebraic Stress Model in a General 3-D Navier-Stokes Method (PAB3D). NASA CR-4702, December 1995.

9. Shih, T-H; Zhu, J.; and Lumley, J. L.: A New Reynolds Stress Algebraic Model. NASA TM-166644, ICOMP 94-8, 1994.

10. Carlson, John R.: A Nozzle Internal Performance Prediction Method, NASA TP-3221, October, 1992.

11. Cahn, Maurice S.: An Experimental Investigation of Sting-Support Effects on Drag and a Comparison With Jet Effects at Transonic Speeds. NACA Report 1353, 1958.

12. Kilgore, Robert A., Adcock, Jerry B., Ray, Edward J.: Flight Simulation Characteristics of the Langley High Reynolds Number Cryogenic Transonic Tunnel. AIAA 74-80, January-February 1974.

13. Patel, V. C.; Rodi, W.; and Scheuerer G.: Turbulence Models for Near-Wall and Low Reynolds Number Flows: A Review. AIAA Journal, Vol. 23, No.9, pp. 1308-1319, September 1985.

14. Gatski, T. B. and Speziale, C. G.: On Explicit Algebraic Stress Models for Complex Turbulent Flows. NASA CR-189725, ICASE Report No. 92-58, November, 1992.

15. Launder, B. E. and Sharma, B. I.: Application of the Energy Dissipation Model of Turbulence to the Calculation of Flow Near a Spinning Disk. Letters in Heat and Mass Transfer, Vol.1, 1974, pp.131-138.

16. Reubush, D. E.: Investigation of Very Low Blockage Ratio Boattail Models in the Langley 16-Foot Transonic Tunnel. NASA TN D-8335, November 1976.

17. Reubush, D. E.: Experimental Study of the Effectiveness of Cylindrical Plume Simulators for Predicting Jet-On Boattail Drag at Mach Numbers up to 1.30. NASA TN D-7795, November 1974.

FIGURES

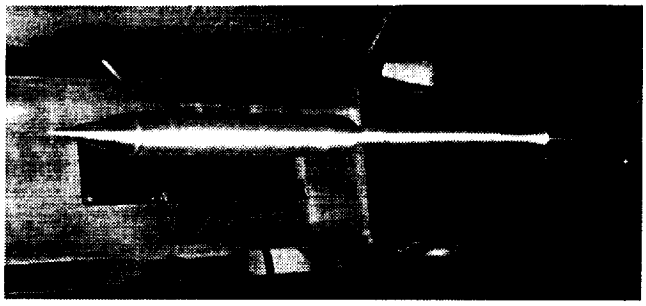

Figure 1.- Model installed in cryogenic tunnel.

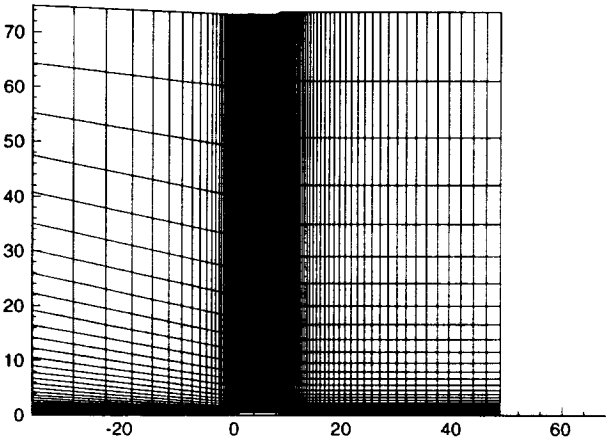

Figure 2.- Overall view of cell centered grid.

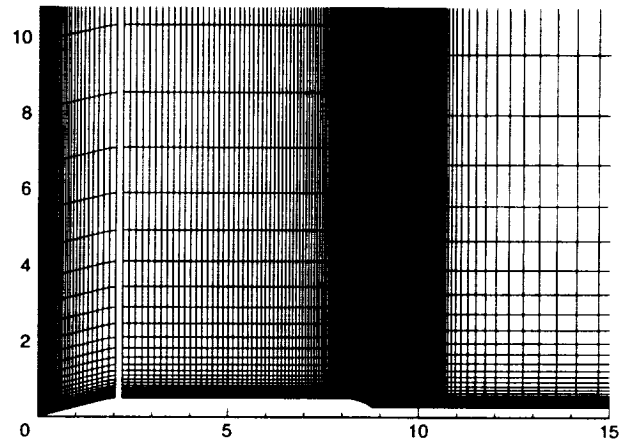

Figure 3.- Cell centered grid for model.

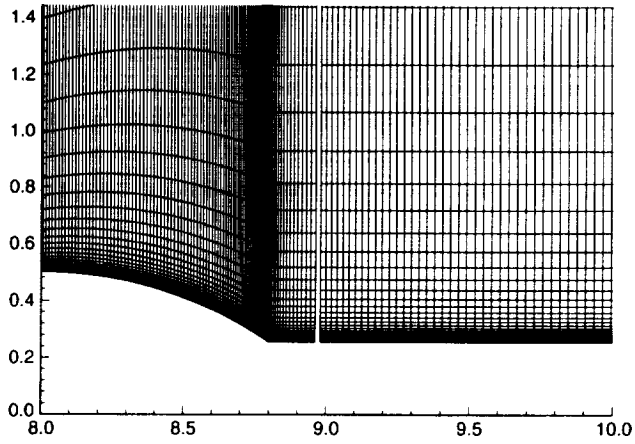

Figure 4.- Detail of afterbody and sting grid.

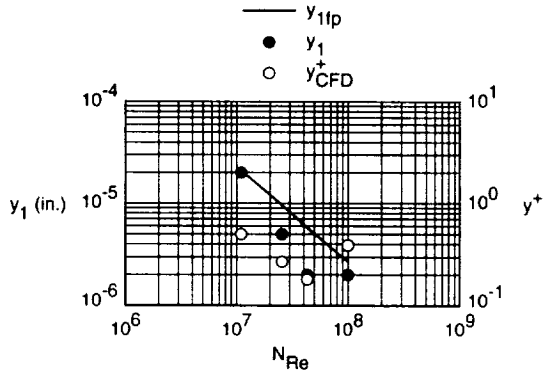

Figure 5.- Variation of first physical cell height (y_1) and y^+ for converged solutions with Reynolds number for freestream conditions of M = 0.6, T_t = 560° R, and model with L/d_m = 8 compared with variation for a 1-D isentropic flat plate.

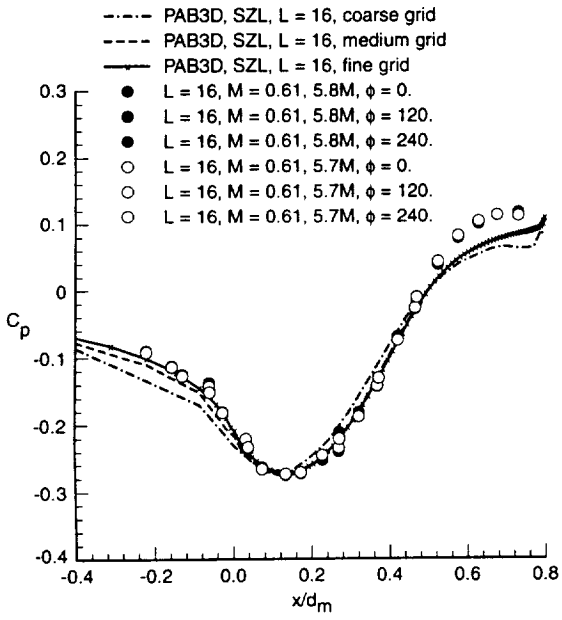

Figure 6.- Comparison of pressure coefficient distributions from solutions at 3 levels of grid density for configuration with $L/d_m = 16$ with experimental data for a Reynolds number of about 5.8 million.

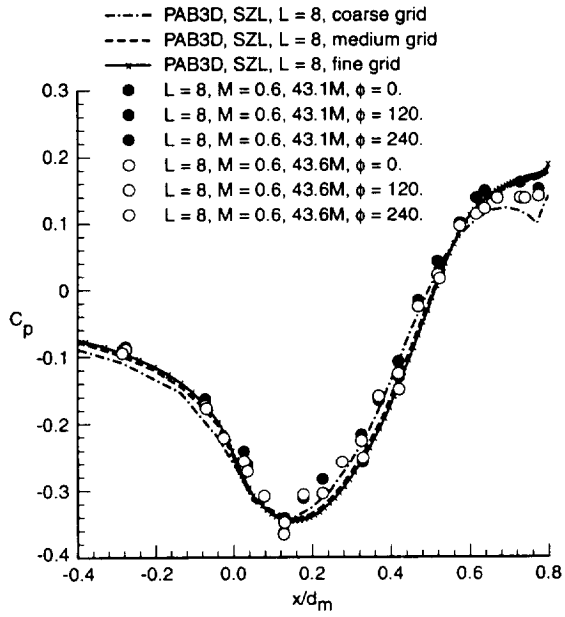

Figure 8.- Comparison of pressure coefficient distributions from solutions at 3 levels of grid density for configuration with $L/d_m = 8$ with experimental data for a Reynolds number of about 43 million.

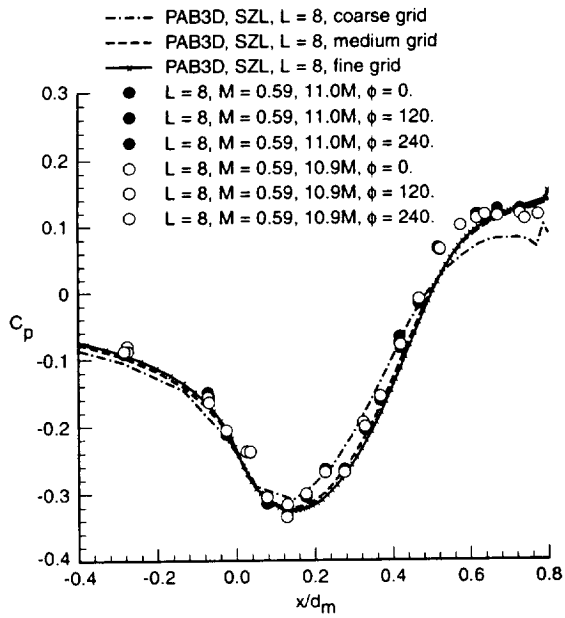

Figure 7.- Comparison of pressure coefficient distributions from solutions at 3 levels of grid density for configuration with $L/d_m = 8$ with experimental data for a Reynolds number of about 11 million.

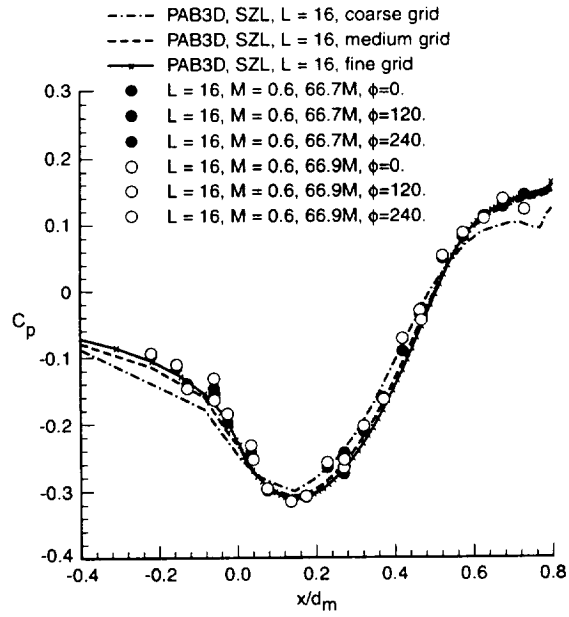

Figure 9.- Comparison of pressure coefficient distributions from solutions at 3 levels of grid density for configuration with $L/d_m = 16$ with experimental data for a Reynolds number of about 67 million.

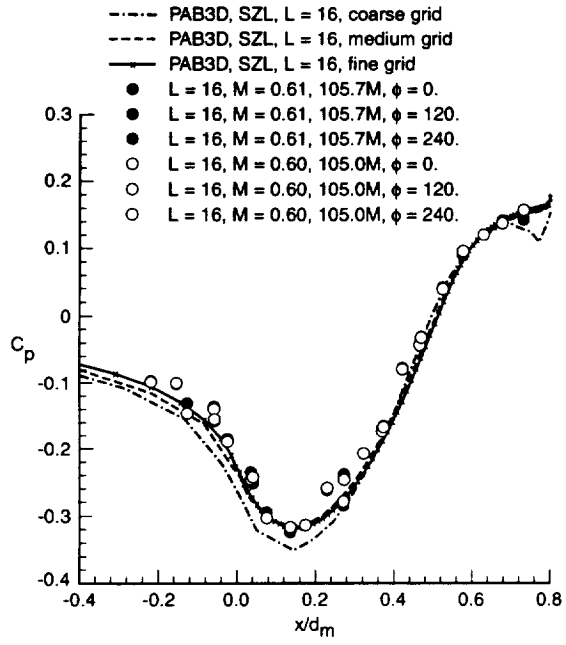

Figure 10.- Comparison of pressure coefficent distributions from solutions at three levels of grid density for configuration with $L/d_m = 16$ with experimental data for a Reynolds number of about 105 million.

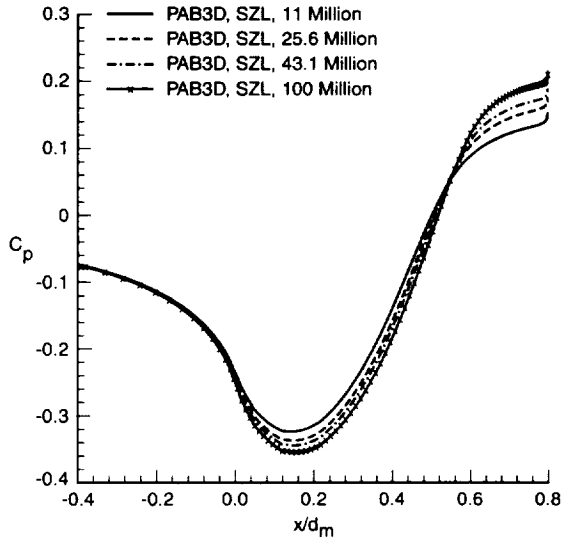

Figure 11.- Comparison of computed pressure coefficient distributions at four Reynolds numbers.

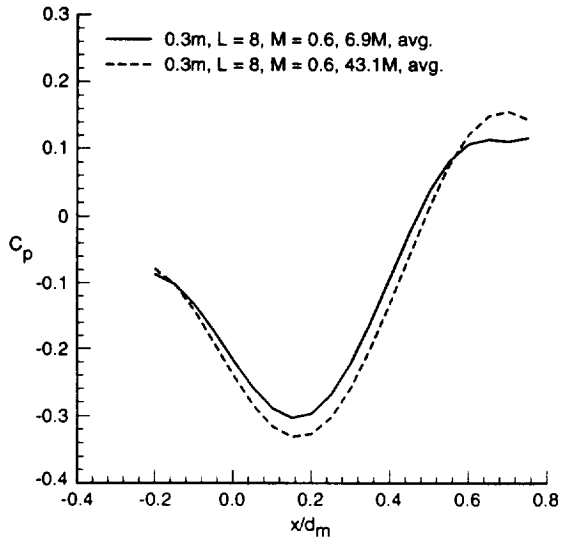

Figure 12.- Comparison of smoothed, averaged experimental pressure coefficient distributions at two Reynolds numbers.

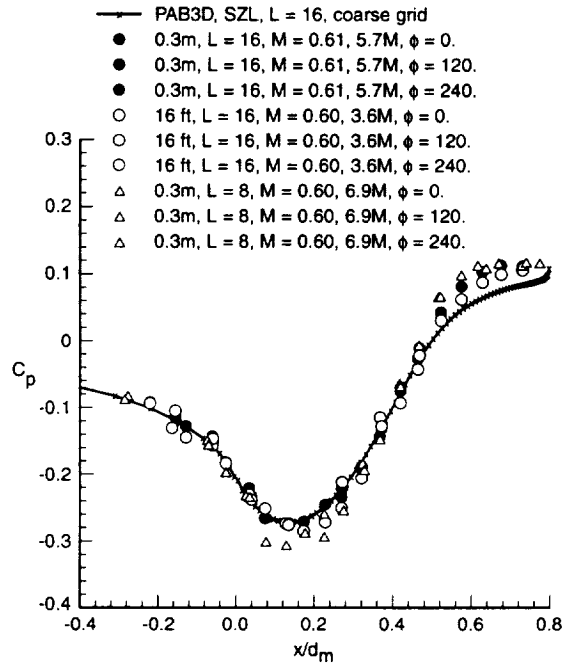

Figure 13.- Comparison of computed pressure coefficient distribution with experimental distributions from both the cryogenic and the 16-Foot Transonic tunnels at Reynolds numbers from 3.6 million to 6.9 million.

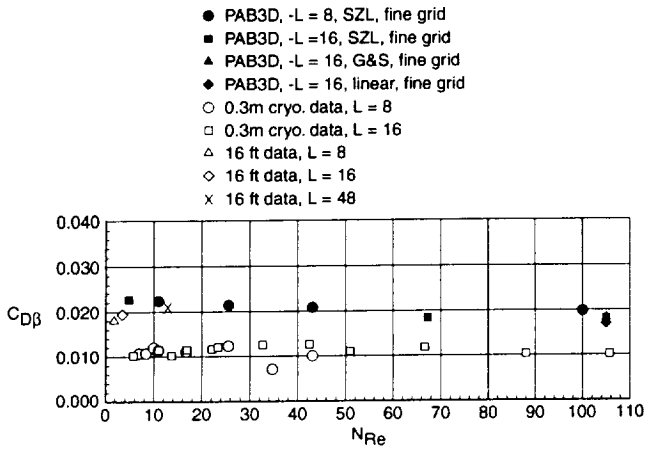

Figure 14.- Comparison of computed afterbody drag coefficient variation with Reynolds number with several sets of experimental data.

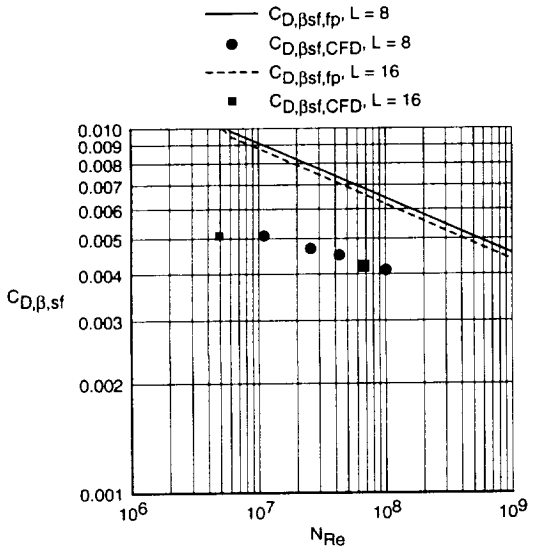

Figure 15.- Comparison of computed afterbody skin friction drag coefficient variation with Reynolds number for both CFD and flat plate methods (used with experimental pressure drag coefficient data).

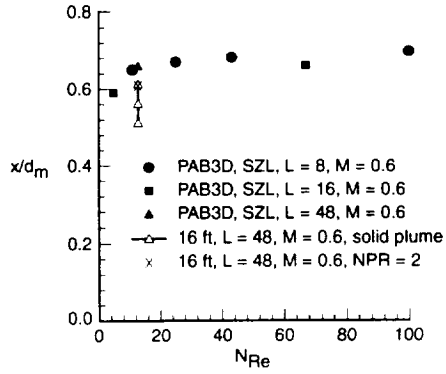

Figure 16.- Comparison of predicted point of flow separation with that obtained from flow visualization in the 16-Foot Transonic Tunnel.

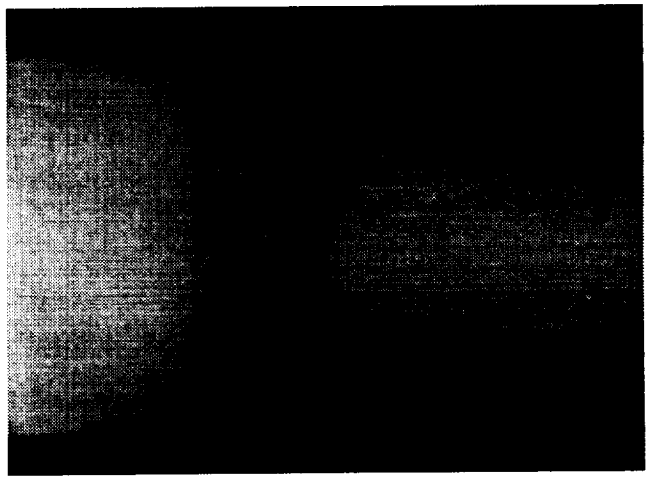

Figure 17.- Oil flow photograph from the 16-Foot Transonic Tunnel.

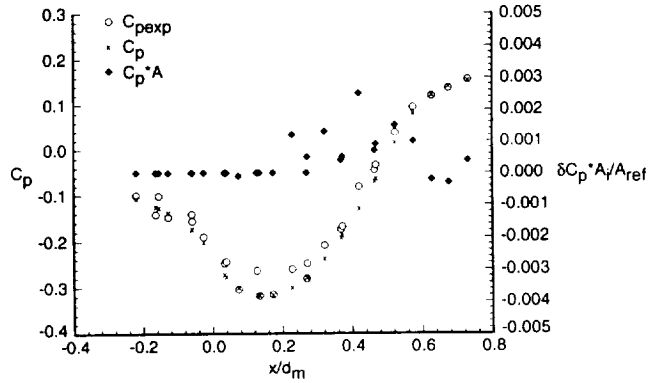

Figure 18.- Comparison of computed and experimental pressure coefficients at the same locations on the afterbody at a Reynolds number of 105 million and an indication of the contributions of the differences to drag coefficient differences.